



OPEN

Well-distributed 1T/2H MoS₂ nanocrystals in the N-doped nanoporous carbon framework by direct pyrolysis

Yalda Tarpoudi Baheri¹, Mahdi Maleki^{1✉}, Hossein Karimian², Jafar Javadpoor¹ & Seyyed Morteza Masoudpanah¹

Molybdenum disulfide (MoS₂) has been a promising anode material in lithium-ion batteries (LIBs) because of its high theoretical capacity and large interlayer spacing. However, its intrinsic poor electrical conductivity and large volume changes during the lithiation/delithiation reactions limit its practical application. An efficient synthesis strategy was developed to prepare the MoS₂ nanocrystals well-anchored into the N-doped nanoporous carbon framework to deal with these challenges by a confined reaction space in an acrylonitrile-based porous polymer during the carbonization process. The prepared hybrid material comprises small 1T/2H-MoS₂ nanoparticles surrounded by a nanoporous carbon matrix. In addition to the highly crystalline nature of the synthesized MoS₂, the low I_D/I_G of the Raman spectrum demonstrated the development of graphitic domains in the carbon support during low-temperature pyrolysis (700 °C). This novel three-dimensional (3D) hierarchical composite shows superior advantages, such as decreased diffusion lengths of lithium ions, preventing the agglomeration of MoS₂ nanocrystals, and maintaining the whole structural stability. The prepared C/MoS₂ hybrid demonstrated fast rate performance and satisfactory cycling stability as an anode material for LIBs.

LIBs have become a primary power sources for portable electronic devices and electric vehicles due to their high energy/power densities, long life cycle, low self-discharge, and high operating voltage^{1–3}. As one of the primary components, the anode material highly determines the LIBs performance. Carbonaceous materials, such as commercial graphite, graphene papers, carbon cloths, carbon nanotubes (CNTs), and carbon nanofibers, are widely utilized as LIBs anodes^{4–7}. However, carbon-based anodes suffer from several drawbacks, such as low theoretical specific capacity, limited rate capability, and safety concerns, restricting LIBs development^{8–11}.

Recent research works have been devoted to introducing novel anode materials with high capacity, reasonable cycle ability, and low cost^{12–16}. Two-dimensional (2D) transition metal-sulfide anode materials with a high specific capacity, low cost, and other interesting properties have attracted considerable attention to be used as the LIBs anodes^{17–19}. Among them, MoS₂ is a promising candidate due to its unique layer structure, large interlayer spacing, weak interlayer van der Waals forces, adjustable band gap, the tailorable density of the active site, and high theoretical capacity (670 mAh g⁻¹)^{20,21}. Nonetheless, the practical application of MoS₂ as a LIBs anode still suffers from drawbacks, including poor electronic/ionic conductivity, substantial volume expansion, and easy stacking/restacking causing fast capacity fading and rate performance deterioration during cycling^{22–25}. The design of the nanostructure hybridization with conductive materials, and elemental doping have been practical solutions to improve the electrochemical performance of MoS₂-based electrode materials^{26–30}. Carbon-based frameworks can considerably enhance the ionic and electronic conductivity of MoS₂^{31–33}.

Hydrothermal (solution synthesis method) and chemical vapor deposition (CVD) procedures are the most frequent approaches for MoS₂ deposition into carbonaceous frameworks as LIBs anodes³⁴. The few-layer MoS₂ vertically anchored on the nitrogen-doped graphene ribbons network has been synthesized through the hydrothermal method. Such composite's convenient structure and high electrical conductivity led to the high electron/ion transfer kinetics and excellent rate capability of 499 mAh g⁻¹ at a high current density of 8.0 A g⁻¹^{32,35}. Furthermore, the porous microspheres constructed from few-layered C/MoS₂ nanosheets produced through a

¹School of Metallurgy and Materials Engineering, Iran University of Science and Technology (IUST), Narmak, Tehran 16846, Iran. ²Department of Chemical Engineering, Golestan University, Aliabad Katoul 45138-15739, Iran. ✉email: malekim@iust.ac.ir

one-pot hydrothermal method exhibited a superior reversible capacity of 752 mAh g⁻¹ at 0.2 A g⁻¹³⁶. The C/MoS₂ hybrid has been also synthesized by a facile hydrothermal procedure using glucose additive as a carbon source in the presence of Mo and S precursors^{37,38}. In the hydrothermal reaction environment, the glucose decomposition led a thin carbon layer formation around the small MoS₂ nanosheets to reduce the diffusion path of lithium ions and speed up the reaction kinetics³⁷. Although hydrothermal procedures are facile processes, it is difficult to deposit homogeneous coating of MoS₂ with strong interfacial bonding and controlled thickness on the surface of the carbon networks³⁹.

CVD methods have been utilized for in-situ grown-MoS₂ layers on prefabricated carbon matrix⁴⁰. The epitaxial growth of MoS₂ nanohorns on the nanotubes (CNTs) network by the CVD method produced a composite with significant electrochemical performance and an excellent specific capacity of 982 mA h g⁻¹ at 0.1 A g⁻¹⁴¹. Graphenes were rolled up into hollow nanotubes, and fine MoS₂ nanosheets were uniformly deposited on the interior surface of nanotubes to construct the MoS₂@graphene nanocables using the CVD method. The prepared freestanding mechanically robust interwoven composite revealed a high specific capacity and excellent cycling performance⁴². However, CVD methods are complicated, costly, and time-consuming to coat the MoS₂ on the carbon supports. Introduction of new deposition methods on the carbon framework without the challenges of the hydrothermal and CVD methods can develop the MoS₂ application in the energy storage fields.

Notably, the morphology of the utilized carbon host and well-distributed MoS₂ in the carbon matrix is insistent on volume change. The sufficient elastic space around the well-distributed MoS₂ can reduce the electrode structure damage and active material detachment from the current collector. Furthermore, large three-interconnected pores can provide enough electrode–electrolyte contacting area⁴³. Porous carbon structures such as graphene, CNTs, and amorphous carbons frameworks have been introduced as a matrix for MoS₂^{44–46}. However, most porous carbon-based hosts are poorly physically contacted with metal sulfides, leading to high charge-transfer resistance and even active materials detachment during cycling.

Therefore, developing well-dispersed MoS₂ nanoparticles with strong interfacial bonding in hierarchical porous carbon frameworks is a straightforward way for obtaining high-performance LIBs anode. Herein, we report a novel method for well-distributed ultra-small MoS₂ nanoparticles (less than 5 nm) in highly interconnected nanoporous carbon through a reaction between sulfur and molybdenum precursors in the confined spaces of a hierarchical polymeric polymerized high internal phase emulsion (polyHIPE). Carbonizing the infiltrated polyHIPE containing potassium persulfate (KPS) and sodium molybdate formed well-distributed and robust anchored small MoS₂ nanoparticles in a carbonaceous bed. The high surface area C/MoS₂ composite (242 m² g⁻¹) revealed high electron/ion transfer kinetics, good cycling stability, and rate capability.

Experimental

Materials. Sodium molybdate (Na₂MoO₄·2H₂O), acrylonitrile (AN), divinylbenzene (DVB), 1,2-dichlorobenzene, benzoyl peroxide (BPO), potassium persulfate (K₂S₂O₈, KPS), and calcium chloride dihydrate (CaCl₂·2H₂O) were purchased from Merck Co. (Darmstadt, Germany). Polyglycerol polyricinoleate (PGPR4150, Palsgaard, Denmark) was kindly given by PishgamanPakhsh Sedigh Co.

PolyHIPE synthesis. AN as a monomer, DVB as a crosslinker, initiator (BPO), and the oil-soluble surfactant PGPR 4150 were added to DCB as the porogenic solvent. The aqueous phase was prepared by adding the CaCl₂·2H₂O and KPS to distilled water. Next, the aqueous phase was added dropwise into the organic phase to prepare the HIPEs. The emulsion was poured into a glass mold and heated at 70 °C for 24 h to obtain the polyHIPE. The polymerized emulsions were then dried at 60 °C for 24 h. The surfactant and unreacted monomers and initiators were extracted by ethanol and water for 24 h in a Soxhlet apparatus. The produced foam was stabilized under air at 240 °C for 8 h.

C/MoS₂ composite synthesis. The prepared stabilized foam was infiltrated by ethanol/water (50/50 Wt%) solution containing sodium molybdate and KPS. Next, impregnated foams were pyrolyzed under a nitrogen atmosphere at 700 °C for 90 min. Figure 1 demonstrates a scheme of the experimental route to obtain the well-distributed ultrasmall 1T/2H MoS₂ nanoparticles in the N-doped nanoporous carbon network.

Characterization

An X'Pert Pro MPD diffractometer (X'Pert Pro MPD, Philips, Germany) was employed to record the X-ray diffraction (XRD) patterns. Nitrogen sorption analysis was measured using a Belsorb instrument at 77 K. To eliminate the adsorbed water and air pollutants, the composites were degassed under vacuum at 150 °C before analysis. X-ray photoelectron spectroscopy (XPS) was carried out with a KRATOS Axis Ultra system equipped with a monochromatized AlK α X-ray source, an aspherical mirror electron analyzer, and a charge neutralization system. SEM micrographs were captured by using a TESCAN VEGA// XMU microscope. A high-resolution transmission electron microscope (JEM-2100, JEOL, Japan) operating at 200 kV has been used for the microstructural investigations. The carbonaceous Au 4f. line (84.2 eV) was employed as the reference to calibrate the binding energies. Raman Spectroscopy was carried out on a Takram micro Raman spectrometer (Teksan™, Iran) equipped with a 532 nm laser as the excitation source at a power of 90 mW. Thermogravimetric analysis (TGA) was performed using a TA Instruments (SDT Q600, TA Instrument Co., USA) at a heating rate of 10 °C min⁻¹ in the air atmosphere.

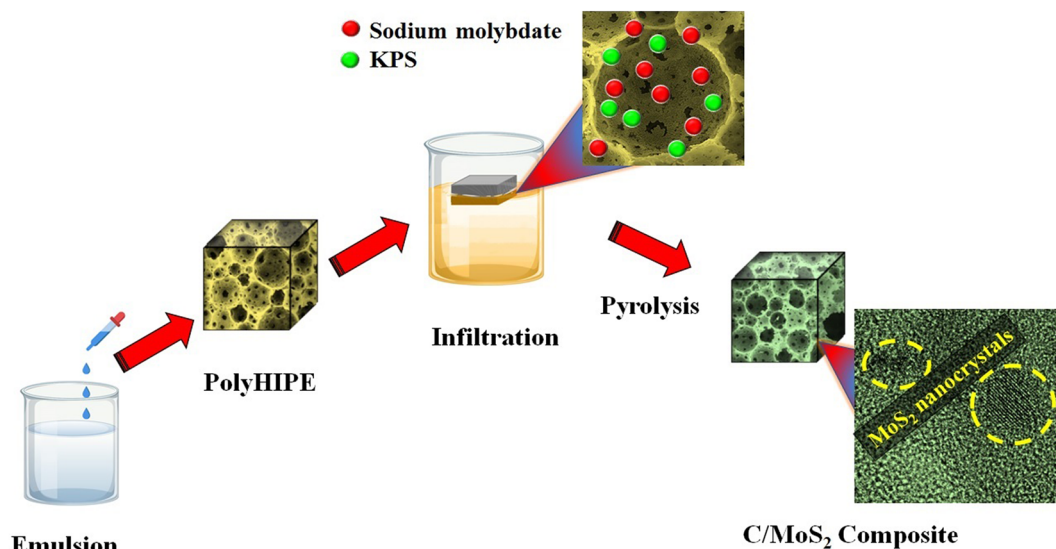


Figure 1. Scheme of the experimental route to obtain the well-distributed ultrasmall 1T/2H MoS₂ nanoparticles in the carbon foam.

Electrochemical performance

The C/MoS₂ composite, polyvinylidene difluoride (PVDF) binder, and conducting carbon (Super P) with a mass ratio of 8:1:1 were added to *N*-methyl-2-pyrrolidone (NMP) to obtain a homogeneous slurry. The slurry was then deposited uniformly on a copper foil. CR2032-type coin cells were assembled in an argon-filled glovebox with metal lithium foil as the reference and counter electrode and Celgard membrane as the separator. A 1.0 M LiPF₆ in ethylene carbonate/dimethyl carbonate (EC/DMC, 1:1 volume ratio) was used as an electrolyte in the coin cell. Charge/discharge cycling was conducted on a computer-controlled Land CT2001A (Wuhan, China) battery tester at different current densities in a potential range of 0.01–3.0 V (vs. Li/Li⁺). The cyclic voltammetry (CV) measurement was conducted at a scan rate of 1 mV s⁻¹ within the range of 0.01–3.0 V on a CH Instrument 600D electrochemical workstation. Electrochemical impedance spectroscopy (EIS) was measured on an electrochemical workstation (VersaSTAT, Princeton Applied Research, USA).

Results and discussion

C/MoS₂ formation. The prepared polyHIPEs were stabilized at 240°C under an air atmosphere for 8 h to obtain the stable polymeric foam to accommodate the molybdenum and sulfur precursor. The SEM micrographs of the stabilized polymeric polyHIPE are shown in Fig. 2a,b. The distributed water droplets in the organic phase during emulsion polymerization led to 3D open cell interconnected porous structure. The measured average size of the cells and windows are 10 and 1 μm, respectively. The inner surface of the cells and windows demonstrates high roughness owing to intensive phase separation between AN and DVB as polymerizable precursors and DCB as the porogenic solvent.

The pyrolysis of the infiltrated stabilized polyHIPE with Na₂MoO₄·2H₂O and KPS led to a black bulk foamy structure. The crystal structure of the composite was investigated with XRD analysis (Fig. 3a). The diffraction peaks at 14.4, 32.5, 39.7, and 58° are respectively referred to the (002), (100), (103), and (110) crystallographic planes of the hexagonal MoS₂ (2H phase, JCPDS No. 37-1492)⁸. In addition to 2H phase reflections, two sharp peaks are observed at low angles of 7.3° and 9.3°. It has been reported that the localization of carbon and nitrogen between MoS₂ atomic layers during its formation led to the enlargement of MoS₂ atomic interlayer spaces^{47–50}. Owing to the presented synthesis procedure, Mo and S precursors can react in an interwoven hierarchical porous structure containing C, O, and N atoms. Therefore, the appearance of low-index peaks can be correlated to the interlayer expansion resulting from small intercalated atoms. Notably, in some research, the emerging peaks at 7.3° and 9.3° have been attributed to the formation of the 1T phase^{51–53}. In addition to MoS₂ peaks, the observed peak at 28.8° could be owing to the MoO₃ hexagonal phase (JCPDS data card no. 21-0569).

Raman spectroscopy was performed to survey the MoS₂ formation and graphitization development in the final composite (Fig. 3b). The broad peak in the range of 395–490 cm⁻¹ is assigned to the 2H-MoS₂ formation. The peak of 447 cm⁻¹ is attributed to second-order Raman scattering 2LA(M) of MoS₂^{52,54}. The peaks at 219 (J₂) and 329 cm⁻¹ (J₃) have been assigned to characteristic peaks of the 1T-MoS₂ phonon mode⁵⁵. The appearance of such peaks has been reported for the as-grown 1T MoS₂ phase in the carbon fiber cloth matrix⁵⁶. The peak appeared in the range of 90–100 cm⁻¹ could be assigned to a vibrational feature in the molybdenum oxide compound detected in the exhibited XRD pattern¹⁰. The presence of an oxide compound has been detected in the exhibited XRD pattern. The Raman spectrum can demonstrate the graphitization degree development in the carbon matrix. As depicted in Fig. 3c, the Raman spectrum displays strong and distinct peaks at 1368 cm⁻¹ and 1592 cm⁻¹, arising from defective carbon bond (D-band) and sp² hybridized carbon (G-band), respectively. The intensity ratio of the D and G bands (I_D/I_G), a common measure to evaluate the quality of graphitization degree

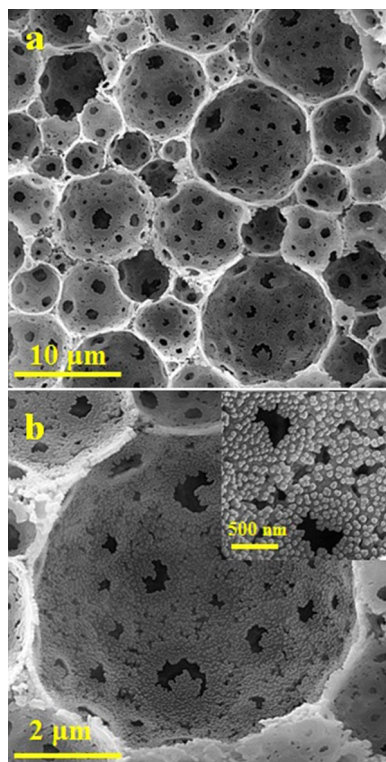


Figure 2. (a,b) SEM micrographs of the stabilized polyHIPE at different magnifications.

in carbonaceous materials, was 0.8, suggesting a noticeable graphitization degree and high crystalline region density. The excellent I_D/I_G ratio for the pyrolyzed sample at the low temperature of 700 °C is a notable finding compared to carbon-based materials synthesized at high temperatures^{57,58}. Further, the broad peak between 2300 and 3250 cm^{-1} could be originated from developed graphitic domains in the microstructure.

The successful formation of MoS_2 in the carbon backbone was also investigated by XPS analysis (Fig. 4). The C 1s spectrum in Fig. 4a was deconvoluted into five peaks at 283.3, 284.1, 285.2, 286.3, and 287.3 eV using a Gaussian profile. The peak centered at 283.3 eV originates from the bonding between Mo and C atoms. The prominent peak with a binding energy of 284.1 eV is attributed to the C=C bonds. The peak at 285.2 eV can be attributed to C-N bonding in the carbon microstructure⁵⁹. Due to the bonding between sulfur and carbon, a peak emerged at 286.3 eV. The peak at 287.3 eV is attributed to C-OH/C-O-Mo bonds or sp^3 carbon in C-O^{37,60}. The Mo 3d spectrum was deconvoluted into six peaks at 226.1, 228.4, 229.2, 231.4, 232.4 and 234.7 eV (Fig. 4b) using a Gaussian profile. The peaks at 228.4 eV and 231.4 eV could be, respectively, assigned to the $3d_{5/2}$ and $3d_{3/2}$ orbits of Mo^{4+} for 2H MoS_2 . The observed peaks at 229.2 eV and 232.4 eV are attributed to $3d_{5/2}$ and $3d_{3/2}$ of the Mo^{4+} for the 1T phase. The peaks appeared at 226.1 eV and 234.7 eV could be related to S 2s and Mo^{6+} , respectively^{61–63}. The deconvolution of the N1s spectrum in Fig. 4c was fitted to four peaks including benzenoid amine (-NH-) or pyrrolic-type (399.4 eV), pyridinic (398.9 eV), quaternary N (401.2 eV), and oxidized N (402.8 eV)⁶⁴. Acrylonitrile, well-known carbon precursor, has been utilized as a one of precursors to prepare the primary polymeric foam. This precursor has a nitrogen in its compound. When the pyrolysis temperature of polyacrylonitrile based polymer is lower than 900 °C, the nitrogen will present in the carbon microstructure^{65,66}.

The N_2 sorption isotherm of the C/ MoS_2 composite is depicted in Fig. 5a. According to International Union of Pure and Applied Chemistry (IUPAC) classification, the isotherm can be categorized as IV isotherm type and H3 hysteresis³. The presence of hysteresis demonstrates the formation of mesopores in the composite structure. The high gas uptake at high relative pressure can be related to big macropores. The BET surface area and pore volume of the C/ MoS_2 composite were 242 $\text{m}^2 \text{g}^{-1}$ and 0.8 $\text{cm}^3 \text{g}^{-1}$, respectively. The BJH pore size distribution of the composite in the inset of Fig. 5 demonstrates the hierarchical porous structure. The high surface area could be due to the highly porous carbon matrix and synthesis procedure. The MoS_2 nanocrystals deposited on carbon-based supports by the hydrothermal method led to a surface area between 10 and 210 $\text{m}^2 \text{g}^{-1}$ ^{167–69}. TGA analysis has been performed under the air atmosphere to determine the MoS_2 content in the composite. As seen in Fig. 5b, weight loss was about 10%, when the temperature increased to 92 °C as a result of physically adsorbed water. The sharp weight loss appeared between 300 and 480 °C. Such weight reduction could be owing to the simultaneous oxidation of carbon to CO_2 and MoS_2 to MoO_3 ^{70–72}. The weight loss diagram shows a stable plateau between 530 and 640 °C which can be probably assigned to the remaining molybdenum oxide (17%). Therefore, the weight fraction of MoS_2 in the composite is about 19%. The next weight reduction is related to the molybdenum oxide sublimation. Therefore, it can be deduced that the amount of MoS_2 in the C/ MoS_2 composite can be about 15%.

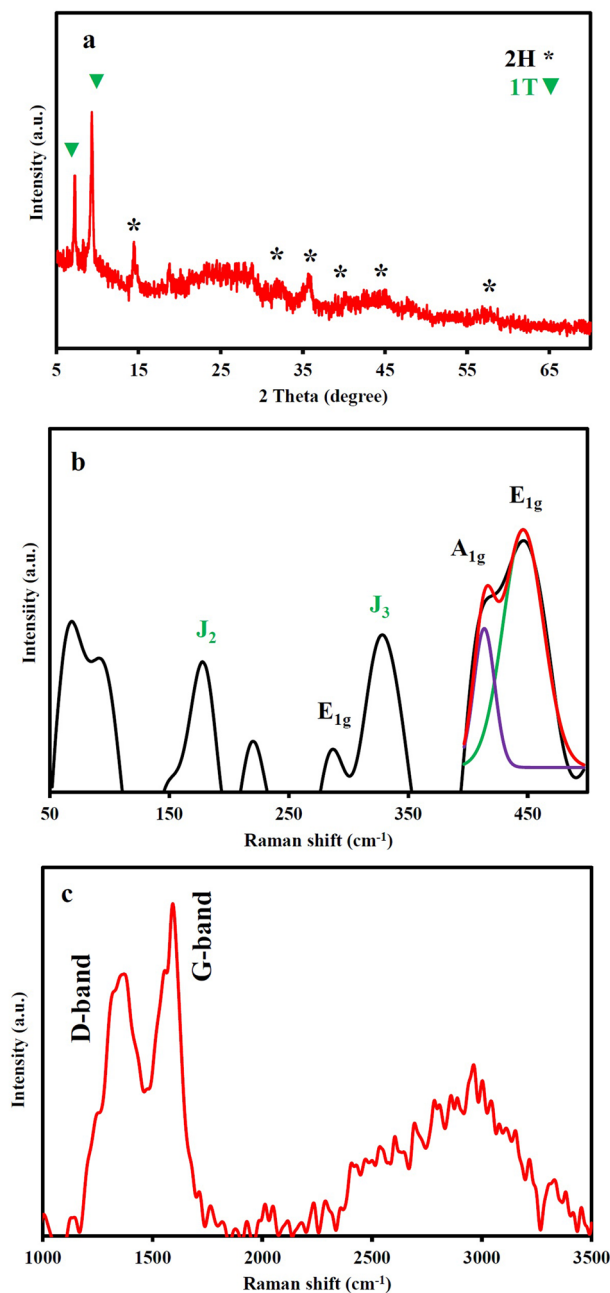


Figure 3. (a) XRD pattern and (b,c) Raman spectra of the prepared composite at 700 °C.

The SEM micrographs of the prepared composite are displayed in Fig. 6a, b. As shown, the carbon framework preserved the primary 3D-interconnected macroporous structure of polymeric foams during pyrolysis at 700 °C. Compared to former polymeric foam, the window and cell in the composite foam show 20 and 15% shrinkage, respectively. As can be seen, the surface of pore walls reveals a high roughness originating from the primary polymeric foam. The infiltration of MoS₂ precursors in the initial polymeric foam shows no adverse effect on the porous carbon matrix structure.

The TEM micrograph of the prepared composite in Fig. 7a displays a hierarchical porous structure confirming the BJH plot of the composite. The nanoporosity can be seen in the carbon microstructure. The well-distributed MoS₂ nanoparticles (less than 10 nm) in the porous carbon matrix in Fig. 7b can be detected. The magnified images of the atomic-resolution image in Fig. 7c, d demonstrate the highly crystalline nature of the MoS₂ nanoparticles. Inset of Fig. 7c displays d-spacing of 0.32 nm consistent with the (004) atomic planes of 2H-MoS₂.

The HAADF-STEM image of the composite in Fig. 8 indicates the excellent dispersion of MoS₂ nanoparticles in the carbon background. Figure 8 shows the EDS elemental maps for C, N, Mo, and S elements, indicating the distribution of the MoS₂ nanoparticles in the carbon microstructure. Furthermore, the nitrogen map demonstrated the presence of this element in the composite microstructure which was confirmed before by XPS analysis.

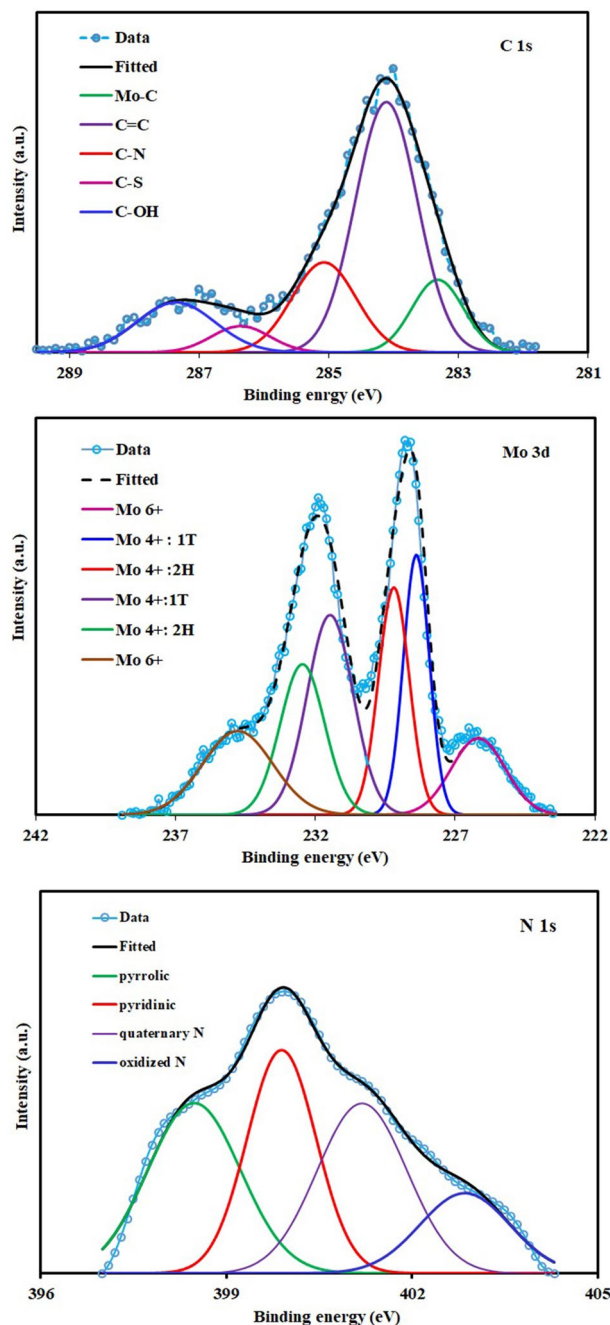


Figure 4. (a) C1s and (b) Mo 3d (c) N 1S XPS spectra of the prepared composite.

Electrochemical performance. The electrochemical performance of the C/MoS₂ composite as anode materials for LIBs was assessed. Figure 9a shows the first three CV curves of the electrode at a scan rate of 1 mV s⁻¹ within a potential range of 0.01–3.0 V. In the first cathodic sweep, three obvious reduction peaks at around 1.2–1.6, 0.66, and 0.53 V can be observed. The former corresponds to the insertion of Li⁺ into MoS₂ interlayers to form Li_xMoS₂. The observed peaks at 0.66 and 0.53 V are attributed to the reduction of Mo²⁺ into the metallic Mo nanoparticles embedded into a Li₂S matrix through the conversion process^{37,73}. During the first anodic scan of the C/MoS₂ electrode, two oxidative peaks at 1.2 V and 2.2 V are observed, which can be assigned to the oxidation of Li₂S into S. In the anodic scanning, an oxidation peak appeared at approximately 2.25 V represents the oxidation reaction from Mo to Mo⁴⁺ and Mo⁶⁺. After the first cycle, the electrode is mainly composed of Mo and S instead of the initial MoS₂. The anodic peaks at 1.4 and 2.3 V overlap with those in the second and third sweeps. During the anodic scan, the oxidation peaks at 1.4 and 2.3 V are the sulfide redox reaction which is related to the partial oxidation of Mo to MoS₂ and the complete formation of MoS₂^{52,74}.

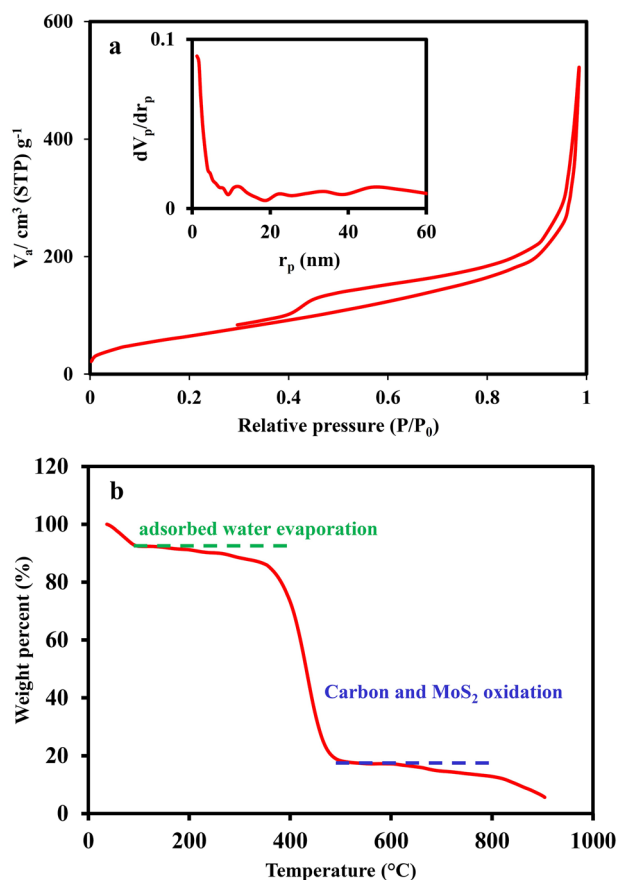


Figure 5. (a) N_2 sorption isotherm and BJH diagram of the prepared C/MoS₂ composite and BJH pore size distribution (inset) (b) TGA diagram of C/MoS₂ composite under air atmosphere.

The electrochemical performance of the C/MoS₂ composite was studied by galvanostatic charge–discharge tests. Figure 9b displays the discharge–charge voltage profiles of the C/MoS₂ composite from the 1st to 5th cycles with a current rate of 0.2 C in the potential window of 0.01–3.0 V (vs. Li/Li⁺). The galvanostatic discharge curve of the C/MoS₂ sample indicated an ultrahigh initial discharge capacity of 1128 mAh g⁻¹. The primary discharge curve shows a short potential plateau between 1.25 and 1.1 V and a long plateau starting from ~1.1 V. The appearance of the short plateau is owing to the irreversible electrolyte decomposition and the solid-electrolyte interphase (SEI) film formation on the composite. Such SEI film formation leads to a fall in charge/discharge capacity⁷⁵. As shown in Fig. 9c, the C/MoS₂ composite electrode demonstrates a stable cycle performance at a current density of 0.2 C. The C/MoS₂ composite preserved a capacity of 554 mAh g⁻¹ across 100 cycles at 0.2 C with a high Coulombic efficiency (~99.5%) (Fig. 9c). Figure 9d depicts the comparison of the rate capability

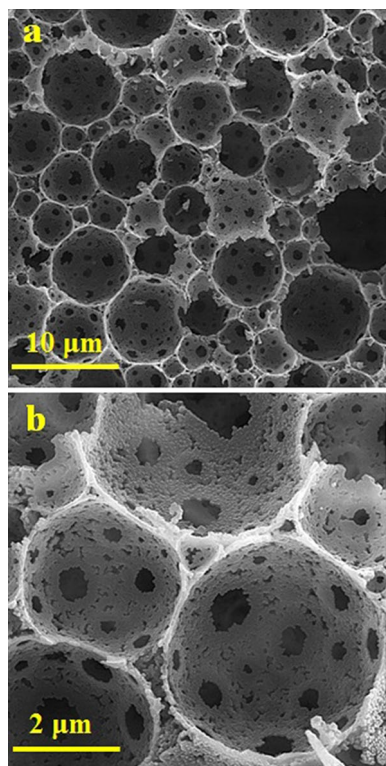


Figure 6. (a,b) SEM micrographs of the obtained C/MoS₂ composite at 700 °C.

of the prepared C/MoS₂ composite. The C/MoS₂ hybrid electrode displays an excellent rate capability of 565, 540, 500, 430, and 370 mAh g⁻¹ at different current densities of 0.1, 0.2, 0.5, 1, 2, and 3 C, respectively. Even at a high current density of 3 C, the C/MoS₂ composite electrode still delivers a high reversible capacity of about 370 mAh g⁻¹. Therefore, the C/MoS₂ composite anode can fast charge/discharge at various applied current densities.

The Nyquist plots in Fig. 9e exhibited a semicircle in the high-frequency region followed by a straight line in the low frequency region. The intercept in the high-frequency region corresponds to the ohmic resistance of the cell (R_c), which combines the total resistance of the electrolyte, separator, and electrical contacts. The diameter of the semicircle is representative of charge transfer resistance (R_{ct}). As can be seen, the R_c value was very low (13 Ω) and R_{ct} was 120 Ω which indicates the quick charge transfer process of the lithium-ion insertion/extraction reaction. The straight line in low frequency representing the Warburg resistance (Z_w) is assigned to the solid-state diffusion resistance of Li ions in the electrode, respectively¹⁷.

The uniform distributed molybdenum and sulfur precursors in initial polyHIPE led to the uniform growth of MoS₂ nanoparticles in the carbon matrix. Further, the hierarchical porous structure of the carbon matrix can provide appropriate channels for electrolyte penetration and ion transportation. The well-dispersed ultrasmall MoS₂ nanoparticles led to the extended electrode/electrolyte interface with highly porous carbon that facilitates ion diffusion into the inner structure of the electrode materials. Despite the low amount of MoS₂ in the composite based on TGA result, MoS₂ pinning on the carbon matrix and strong interactions between the MoS₂ and carbon components prevent the MoS₂ restacking and the stability enhancement of the C/MoS₂. Furthermore, the carbon template prevented the overgrowth and aggregation of MoS₂ into bulk materials during the cycling process.

Conclusion

Herein a novel strategy was developed to grow the 1T/2H-MoS₂ nanocrystals in the N-doped nanoporous carbon. The pyrolysis of sodium molybdate and KPS in the acrylonitrile-based polymer backbone led to the formation of the pinned ultrasmall MoS₂ nanoparticle in the highly porous carbon matrix. The high surface area of the hybrid structure led to a short lithium diffusion path and easier lithiation/delithiation in the microstructure. The C/MoS₂ composite delivered a high initial capacity of 556 mAh g⁻¹ at 0.2 A g⁻¹, and its capacity was maintained even after 100 cycles, showing high cycling stability.

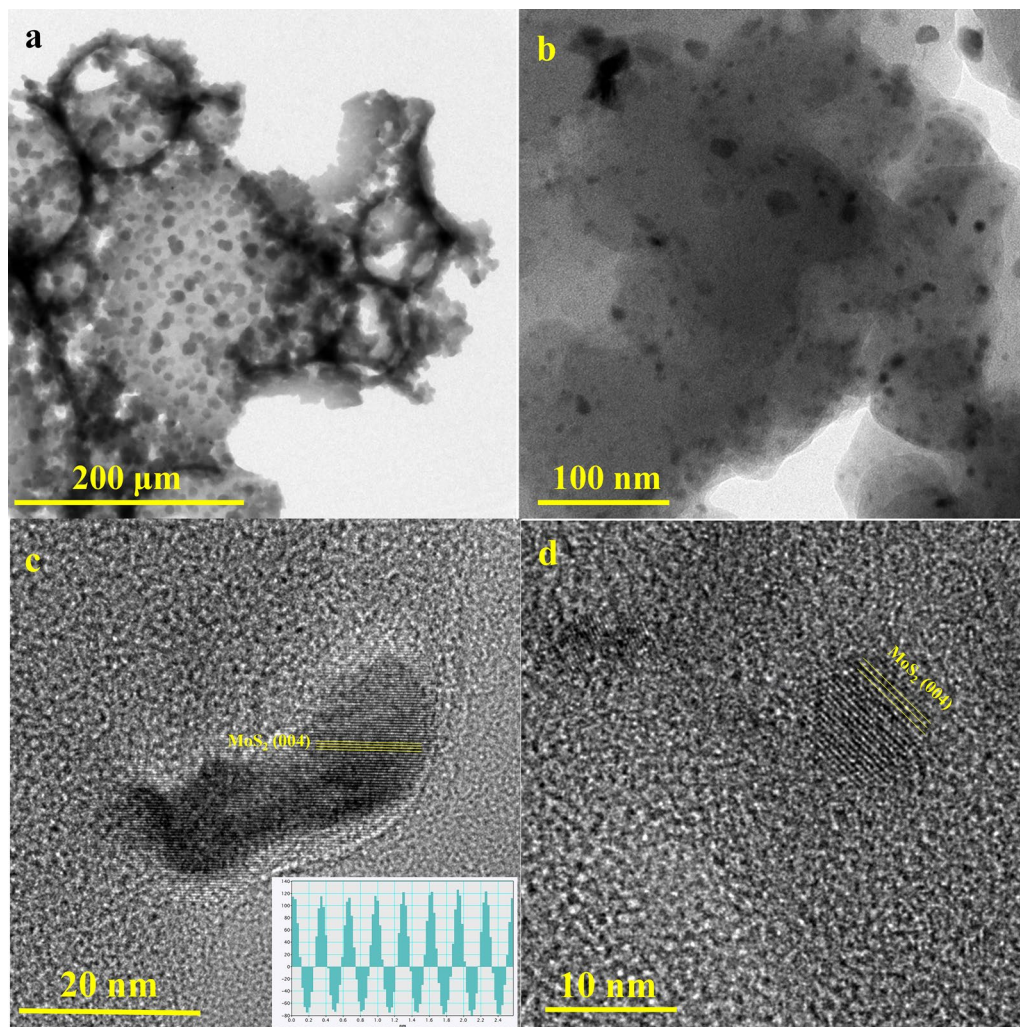


Figure 7. (a) TEM micrograph of the porous C/MoS₂ composite (b) well-distribution of MoS₂ distribution in carbon matrix, and (c,d) MoS₂ nanoparticles crystallinity [inset of (c) shows d-spacing of MoS₂ nanoparticles].

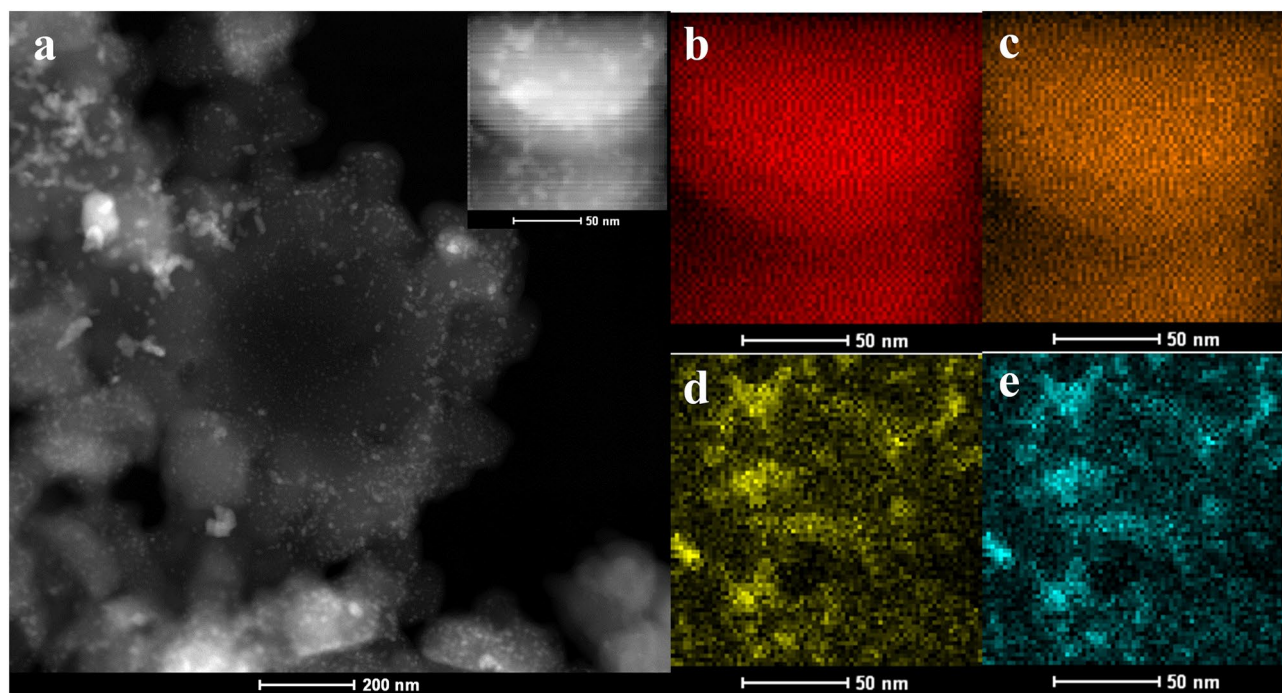


Figure 8. (a) HAADF-STEM and TEM image of C/MoS₂ (inset) and (b) C, (c) N, (d) Mo, and (e) S elemental mapping images.

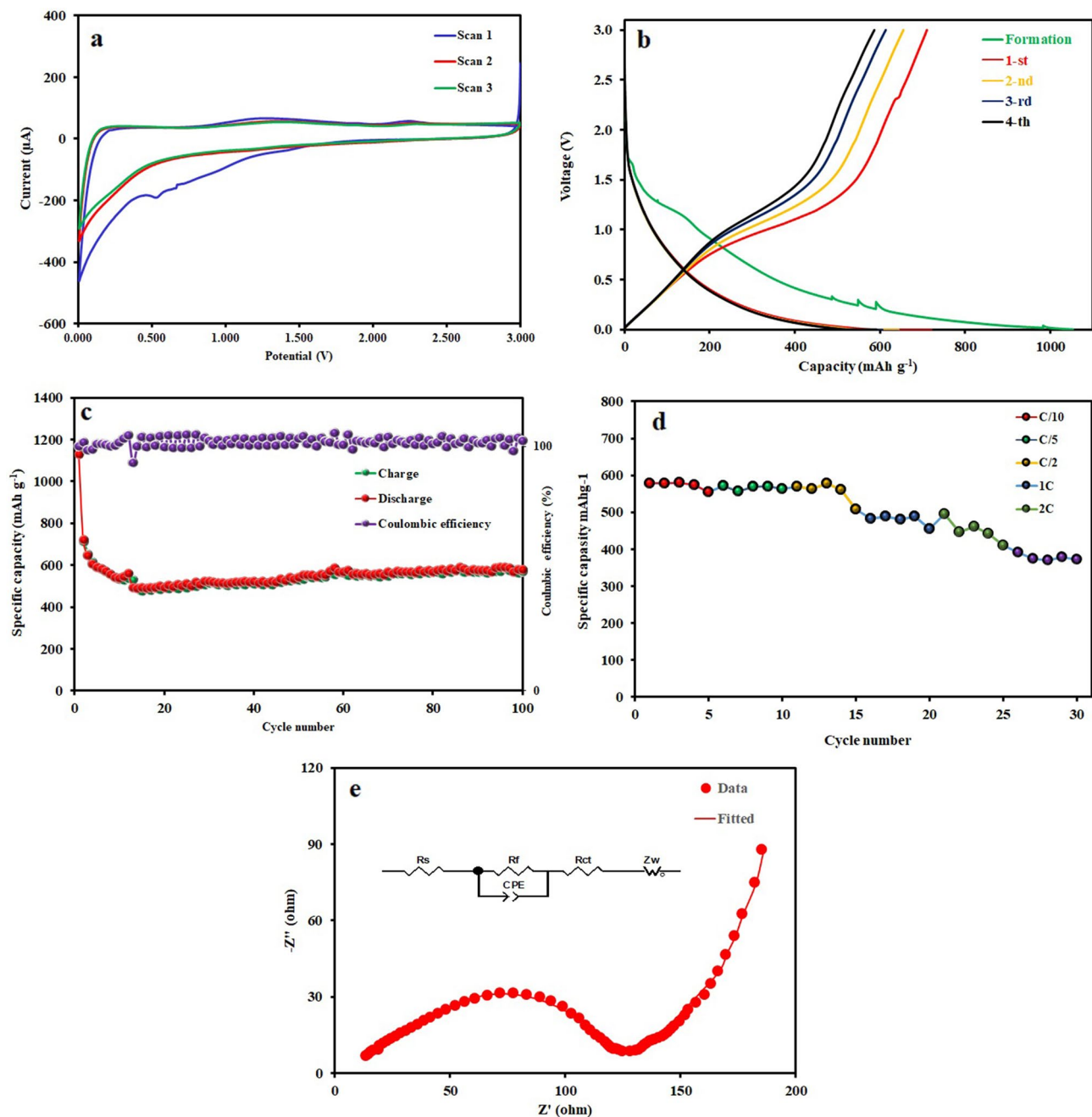


Figure 9. (a) The first three CV curves tested at a scan rate of 1 mV s^{-1} , (b) discharge–charge voltage profiles from the 1st to 5th cycles with a current rate of 0.2 C in the potential window of 0.01–3.0 V (vs. Li/Li⁺), (c) cycle performance, and (d) rate capability, and (e) electrochemical impedance spectra and equivalent circuit model of the C/MoS₂ composite.

Data availability

The datasets used and/or analyzed during the current study available from the corresponding author on reasonable request.

Received: 16 January 2023; Accepted: 3 May 2023

Published online: 09 May 2023

References

- Zhang, G. *et al.* Internal short circuit mechanisms, experimental approaches and detection methods of lithium-ion batteries for electric vehicles: A review. *Renew. Sustain. Energy Rev.* **141**, 110790 (2021).
- Liu, J. *et al.* A review of performance attenuation and mitigation strategies of lithium-ion batteries. *Adv. Funct. Mater.* **32**(8), 2107769 (2022).
- Yadlapalli, R. T. *et al.* A review on energy efficient technologies for electric vehicle applications. *J. Energy Storage* **50**, 104212 (2022).

4. Dao, T. D. *et al.* Super-tough functionalized graphene paper as a high-capacity anode for lithium ion batteries. *Chem. Eng. J.* **250**, 257–266 (2014).
5. Tang, X. *et al.* CNT boosted two-dimensional flaky metal-organic nanosheets for superior lithium and potassium storage. *Chem. Eng. J.* **430**, 133023 (2022).
6. Syum, Z. *et al.* Superior lithium-ion storage performance of hierarchical tin disulfide and carbon nanotube-carbon cloth composites. *J. Power Sources* **482**, 228923 (2021).
7. Kim, H. *et al.* Novel hybrid carbon nanofiber/highly branched graphene nanosheet for anode materials in lithium-ion batteries. *ACS Appl. Mater. Interfaces.* **6**(21), 18590–18596 (2014).
8. Nzereogu, P. U. *et al.* Anode materials for lithium-ion batteries: A review. *Appl. Surf. Sci. Adv.* **9**, 100233 (2022).
9. Bondarde, M.P. *et al.* 23—Carbon-based anode materials for lithium-ion batteries. in *Lithium-Sulfur Batteries* (Gupta, R.K. *et al.* Eds.). 521–545 (Elsevier, 2022).
10. Bi, H. *et al.* Three-dimensional porous graphene-like carbon cloth from cotton as a free-standing lithium-ion battery anode. *J. Mater. Chem. A* **4**(30), 11762–11767 (2016).
11. Maleki, M. *et al.* Non-graphitizable resin coating on polyacrylonitrile-based polyHIPE to prepare high surface area graphitic carbon foam and the investigation of its electrochemical performance as an anode of lithium-ion batteries. *J. Alloy. Compd.* **873**, 159771 (2021).
12. Zhou, Y. *et al.* Molybdenum chalcogenides based anode materials for alkali metal ions batteries: Beyond lithium ion batteries. *Energy Storage Mater.* **50**, 308–333 (2022).
13. Liu, Z. *et al.* Silicon oxides: A promising family of anode materials for lithium-ion batteries. *Chem. Soc. Rev.* **48**(1), 285–309 (2019).
14. Thakur, A. K. *et al.* Advancement in graphene-based nanocomposites as high capacity anode materials for sodium-ion batteries. *J. Mater. Chem. A* **9**(5), 2628–2661 (2021).
15. Oh, H. G. & Park, S.-K. Co-MOF derived MoSe₂@CoSe₂/N-doped carbon nanorods as high-performance anode materials for potassium ion batteries. *Int. J. Energy Res.* **46**(8), 10677–10688 (2022).
16. JinJang, Y. & Park, S.-K. Rational design of hierarchical Ni-Mo bimetallic Selenide/N-doped carbon microspheres toward high-performance potassium ion batteries. *Appl. Surf. Sci.* **583**, 152491 (2022).
17. Geng, P. *et al.* Transition metal sulfides based on graphene for electrochemical energy storage. *Adv. Energy Mater.* **8**(15), 1703259 (2018).
18. Xu, X. *et al.* Nanostructured transition metal sulfides for lithium ion batteries: Progress and challenges. *Nano Today* **9**(5), 604–630 (2014).
19. Wang, J. *et al.* MOFs-derived transition metal sulfide composites for advanced sodium ion batteries. *Energy Storage Mater.* **41**, 404–426 (2021).
20. Jiang, J. *et al.* Engineering ultrathin MoS₂ nanosheets anchored on N-doped carbon microspheres with pseudocapacitive properties for high-performance lithium-ion capacitors. *Small Methods* **3**(7), 1900081 (2019).
21. Wang, F. *et al.* S, N co-doped carbon nanotubes decorated with ultrathin molybdenum disulfide nanosheets with highly electrochemical performance. *Nanoscale* **9**(19), 6346–6352 (2017).
22. Chang, K. & Chen, W. l-Cysteine-assisted synthesis of layered MoS₂/graphene composites with excellent electrochemical performances for lithium ion batteries. *ACS Nano* **5**(6), 4720–4728 (2011).
23. Zhang, J. *et al.* Encapsulating carbon-coated MoS₂ nanosheets within a nitrogen-doped graphene network for high-performance potassium-ion storage. *Adv. Mater. Interfaces* **6**(22), 1901066 (2019).
24. Ye, B. *et al.* Encapsulation of 2D MoS₂ nanosheets into 1D carbon nanobelts as anodes with enhanced lithium/sodium storage properties. *J. Mater. Chem. C* **10**(9), 3329–3342 (2022).
25. Liu, X. *et al.* A MoS₂/carbon hybrid anode for high-performance Li-ion batteries at low temperature. *Nano Energy* **70**, 104550 (2020).
26. Liu, Z. *et al.* Unveiling the relationship between the multilayer structure of metallic MoS₂ and the cycling performance for lithium ion batteries. *Nanoscale* **14**(24), 8621–8627 (2022).
27. Zhu, S. *et al.* In situ architecting endogenous heterojunction of MoS₂ coupling with Mo₂CT_x MXenes for optimized Li⁺ storage. *Adv. Mater.* **34**(5), 2108809 (2022).
28. Lan, B. *et al.* Constructing highly stable lithium storage materials by improving the bond strength of MoS₂ to graphene via chitosan. *Carbon* **192**, 384–394 (2022).
29. Xin, D. *et al.* Co-doped 1T-MoS₂ nanosheets anchored on carbon cloth as self-supporting anode for high-performance lithium storage. *J. Alloy. Compd.* **921**, 166099 (2022).
30. Li, M. *et al.* Vanadium doped 1T MoS₂ nanosheets for highly efficient electrocatalytic hydrogen evolution in both acidic and alkaline solutions. *Chem. Eng. J.* **409**, 128158 (2021).
31. Wei, Z. *et al.* Covalent pinning of highly dispersed ultrathin metallic-phase molybdenum disulfide nanosheets on the inner surface of mesoporous carbon spheres for durable and rapid sodium storage. *ACS Appl. Mater. Interfaces.* **13**(49), 58652–58664 (2021).
32. Zhang, C.-L. *et al.* MoS₂ nanoplates assembled on electrospun polyacrylonitrile-metal organic framework-derived carbon fibers for lithium storage. *Nano Energy* **61**, 104–110 (2019).
33. Wang, H. *et al.* Few-layer MoS₂ nanosheets incorporated into hierarchical porous carbon for lithium-ion batteries. *Chem. Eng. J.* **288**, 179–184 (2016).
34. Jiang, J. *et al.* Engineering Ultrathin MoS₂ Nanosheets Anchored on N-Doped Carbon Microspheres with Pseudocapacitive Properties for High-Performance Lithium-Ion Capacitors. Vol. 3(7). 1900081 (2019).
35. Xiao, Z. *et al.* Nitrogen-doped graphene ribbons/MoS₂ with ultrafast electron and ion transport for high-rate Li-ion batteries. *Chem. Eng. J.* **408**, 127269 (2021).
36. Chen, B. *et al.* Facile synthesis and electrochemical properties of continuous porous spheres assembled from defect-rich, interlayer-expanded, and few-layered MoS₂/C nanosheets for reversible lithium storage. *J. Power Sources* **387**, 16–23 (2018).
37. Bai, J. *et al.* Glucose-induced synthesis of 1T-MoS₂/C hybrid for high-rate lithium-ion batteries. *Small* **15**(14), 1805420 (2019).
38. Ding, S., Chen, J. S. & Lou, X. W. Glucose-assisted growth of MoS₂ nanosheets on CNT backbone for improved lithium storage properties. *Chem. Eur. J.* **17**(47), 13142–13145 (2011).
39. Wang, J.-G. *et al.* Onion-like nanospheres organized by carbon encapsulated few-layer MoS₂ nanosheets with enhanced lithium storage performance. *J. Power Sources* **413**, 327–333 (2019).
40. Schmidt, H. *et al.* Transport properties of monolayer MoS₂ grown by chemical vapor deposition. *Nano Lett.* **14**(4), 1909–1913 (2014).
41. Zhang, Z. *et al.* Carbon-Sheathed MoS₂ Nanothorns Epitaxially Grown on CNTs: Electrochemical Application for Highly Stable and Ultrafast Lithium Storage. Vol. 8(7). 1700174 (2018).
42. Kong, D. *et al.* Rational design of MoS₂@graphene nanocables: Towards high performance electrode materials for lithium ion batteries. *Energy Environ. Sci.* **7**(10), 3320–3325 (2014).
43. Zhou, X.-H. *et al.* Locking metal sulfide nanoparticles in interconnected porous carbon nanofibers with protective macro-porous skin as freestanding anodes for lithium ion batteries. *Chem. Eng. J.* **397**, 125271 (2020).
44. Wang, J. *et al.* Double-phase 1T/2H-MoS₂ heterostructure loaded in N-doped carbon/CNT complex carbon for efficient and rapid lithium storage. *Mater. Today Energy* **29**, 101103 (2022).

45. Zhao, J. *et al.* The application of nanostructured transition metal sulfides as anodes for lithium ion batteries. *J. Energy Chem.* **27**(6), 1536–1554 (2018).
46. Dinh, D. A. *et al.* Defect-free MoS₂-flakes/amorphous-carbon hybrid as an advanced anode for lithium-ion batteries. *Energy Fuels* **35**(4), 3459–3468 (2021).
47. Wang, D. *et al.* Swollen ammoniated MoS₂ with 1T/2H hybrid phases for high-rate electrochemical energy storage. *ACS Sustain. Chem. Eng.* **5**(3), 2509–2515 (2017).
48. Wei, J. *et al.* Conversion of 2H MoS₂ to 1 T MoS₂ via lithium ion doping: Effective removal of elemental mercury. *Chem. Eng. J.* **428**, 131014 (2022).
49. Lu, X. *et al.* Intercalation of coordination polymer to regulate interlayer of 2D layered MoS₂ for hydrogen evolution reaction. *Int. J. Hydrogen Energy* **47**(42), 18347–18356 (2022).
50. Venkateshwaran, S., Josline, M. J. & Senthil Kumar, S. M. Fine-tuning interlayer spacing in MoS₂ for enriching 1T phase via alkylated ammonium ions for electrocatalytic hydrogen evolution reaction. *Int. J. Hydrogen Energy.* **46**(12), 8377–8390 (2021).
51. Wu, J. *et al.* Dual-phase MoS₂ as a high-performance sodium-ion battery anode. *J. Mater. Chem. A* **8**(4), 2114–2122 (2020).
52. Wu, M. *et al.* Metallic 1T MoS₂ nanosheet arrays vertically grown on activated carbon fiber cloth for enhanced Li-ion storage performance. *J. Mater. Chem. A* **5**(27), 14061–14069 (2017).
53. Sarma, S. & Ray, S. C. Trigonal (1T) and hexagonal (2H) mixed phases MoS₂ thin films. *Appl. Surf. Sci.* **474**, 227–231 (2019).
54. Lei, Z. *et al.* Thermally stable fishnet-like 1T-MoS₂/CNT heterostructures with improved electrode performance. *J. Mater. Chem. A* **9**(8), 4707–4715 (2021).
55. Jiao, Y. *et al.* Ion transport nanotube assembled with vertically aligned metallic MoS₂ for high rate lithium-ion batteries. *Adv. Energy Mater.* **8**(15), 1702779 (2018).
56. Tang, W.-J. *et al.* Hollow metallic 1T MoS₂ arrays grown on carbon cloth: A freestanding electrode for sodium ion batteries. *J. Mater. Chem. A* **6**(37), 18318–18324 (2018).
57. Maleki, M. *et al.* Development of graphitic domains in carbon foams for high efficient electro/photo-to-thermal energy conversion phase change composites. *Chem. Eng. J.* **362**, 469–481 (2019).
58. Beitollahi, A. & Sheikholeslami, M. A. S. A novel approach for development of graphene structure in mesoporous carbon of high specific surface area. *Carbon* **107**, 440–447 (2016).
59. Lei, Z. *et al.* Strong coupling of MoS₂ nanosheets and nitrogen-doped graphene for high-performance pseudocapacitance lithium storage. *Small* **14**(25), 1704410 (2018).
60. Zhao, C. *et al.* Self-assembly-induced alternately stacked single-layer MoS₂ and N-doped graphene: A novel van der Waals heterostructure for lithium-ion batteries. *ACS Appl. Mater. Interfaces.* **8**(3), 2372–2379 (2016).
61. Niu, H. *et al.* Structurally stable ultrathin 1T–2H MoS₂ heterostructures coaxially aligned on carbon nanofibers toward superhigh-energy-density supercapacitor and enhanced electrocatalysis. *Chem. Eng. J.* **399**, 125672 (2020).
62. Xiang, T. *et al.* Vertical 1T-MoS₂ nanosheets with expanded interlayer spacing edged on a graphene frame for high rate lithium-ion batteries. *Nanoscale* **9**(21), 6975–6983 (2017).
63. Zheng, X. *et al.* Flexible MoS₂@electrospun PVDF hybrid membrane as advanced anode for lithium storage. *Chem. Eng. J.* **370**, 547–555 (2019).
64. BannaMotejaddedEmrooz, H., Maleki, M. & Rahmani, A. Azolla-derived hierarchical nanoporous carbons: From environmental concerns to industrial opportunities. *J. Taiwan Inst. Chem. Eng.* **91**, 281–290 (2018).
65. Khayyam, H. *et al.* PAN precursor fabrication, applications and thermal stabilization process in carbon fiber production: Experimental and mathematical modelling. *Prog. Mater. Sci.* **107**, 100575 (2020).
66. Ra, E. J. *et al.* High power supercapacitors using polyacrylonitrile-based carbon nanofiber paper. *Carbon* **47**(13), 2984–2992 (2009).
67. Rajapriya, A. *et al.* Direct growth of MoS₂ hierarchical nanoflowers on electrospun carbon nanofibers as an electrode material for high-performance supercapacitors. *J. Alloy. Compd.* **859**, 157771 (2021).
68. Zhang, H.-J., Jia, Q.-C. & Kong, L.-B. Multi-dimensional hybrid heterostructure MoS₂@C nanocomposite as a highly reversible anode for high-energy lithium-ion capacitors. *Appl. Surf. Sci.* **531**, 147222 (2020).
69. Luo, X. *et al.* One-pot hydrothermal synthesis of MoS₂ anchored corncob-derived carbon nanospheres for use as a high-capacity anode for reversible Li-ion battery. *J. Solid State Chem.* **296**, 122020 (2021).
70. Pan, F. *et al.* MoS₂-graphene nanosheet-CNT hybrids with excellent electrochemical performances for lithium-ion batteries. *RSC Adv.* **5**(95), 77518–77526 (2015).
71. Hou, M. *et al.* Aging mechanism of MoS₂ nanosheets confined in N-doped mesoporous carbon spheres for sodium-ion batteries. *Nano Energy* **62**, 299–309 (2019).
72. Zhang, Y. *et al.* Vertically oxygen-incorporated MoS₂ nanosheets coated on carbon fibers for sodium-ion batteries. *ACS Appl. Mater. Interfaces* **10**(41), 35206–35215 (2018).
73. Liu, X. *et al.* Heteroarchitecturing a novel three-dimensional hierarchical MoO₂/MoS₂/carbon electrode material for high-energy and long-life lithium storage. *J. Mater. Chem. A* **9**(22), 13001–13007 (2021).
74. Cui, C. *et al.* Growth of MoS₂@C nanobowls as a lithium-ion battery anode material. *RSC Adv.* **5**(112), 92506–92514 (2015).
75. Michan, A. L., Leskes, M. & Grey, C. P. Voltage dependent solid electrolyte interphase formation in silicon electrodes: Monitoring the formation of organic decomposition products. *Chem. Mater.* **28**(1), 385–398 (2016).

Author contributions

Y.T.B.; Experimental work, Visualization, Investigation, Writing. M.M.; Supervision, Conceptualization, Visualization, Investigation. H.K.; Polymer synthesis, Writing- Original draft preparation. J.J.; Supervision, Conceptualization, Writing-Original draft preparation. S.M.M., Battery consideration, Visualization, Conceptualization.

Competing interests

The authors declare no competing interests.

Additional information

Correspondence and requests for materials should be addressed to M.M.

Reprints and permissions information is available at www.nature.com/reprints.

Publisher's note Springer Nature remains neutral with regard to jurisdictional claims in published maps and institutional affiliations.



Open Access This article is licensed under a Creative Commons Attribution 4.0 International License, which permits use, sharing, adaptation, distribution and reproduction in any medium or format, as long as you give appropriate credit to the original author(s) and the source, provide a link to the Creative Commons licence, and indicate if changes were made. The images or other third party material in this article are included in the article's Creative Commons licence, unless indicated otherwise in a credit line to the material. If material is not included in the article's Creative Commons licence and your intended use is not permitted by statutory regulation or exceeds the permitted use, you will need to obtain permission directly from the copyright holder. To view a copy of this licence, visit <http://creativecommons.org/licenses/by/4.0/>.

© The Author(s) 2023